Journal of Biomedical Optics

BiomedicalOptics.SPIEDigitalLibrary.org

Correcting for targeted and control agent signal differences in paired-agent molecular imaging of cancer cell-surface receptors

Negar Sadeghipour
Scott C. Davis
Kenneth M. Tichauer

SPIE.

Negar Sadeghipour, Scott C. Davis, Kenneth M. Tichauer, "Correcting for targeted and control agent signal differences in paired-agent molecular imaging of cancer cell-surface receptors," *J. Biomed. Opt.* **23**(6), 066004 (2018), doi: 10.1117/1.JBO.23.6.066004.

Correcting for targeted and control agent signal differences in paired-agent molecular imaging of cancer cell-surface receptors

Negar Sadeghipour,[a] Scott C. Davis,[b] and Kenneth M. Tichauer[a,*]
[a]Illinois Institute of Technology, Biomedical Engineering, Chicago, Illinois, United States
[b]Thayer School of Engineering, Dartmouth College, Hanover, New Hampshire, United States

Abstract. Paired-agent kinetic modeling protocols provide one means of estimating cancer cell-surface receptors with *in vivo* molecular imaging. The protocols employ the coadministration of a control imaging agent with one or more targeted imaging agent to account for the nonspecific uptake and retention of the targeted agent. These methods require the targeted and control agent data be converted to equivalent units of concentration, typically requiring specialized equipment and calibration, and/or complex algorithms that raise the barrier to adoption. This work evaluates a kinetic model capable of correcting for targeted and control agent signal differences. This approach was compared with an existing simplified paired-agent model (SPAM), and modified SPAM that accounts for signal differences by early time point normalization of targeted and control signals ($SPAM_{PN}$). The scaling factor model ($SPAM_{SF}$) outperformed both SPAM and $SPAM_{PN}$ in terms of accuracy and precision when the scale differences between targeted and imaging agent signals (α) were not equal to 1, and it matched the performance of SPAM for $\alpha = 1$. This model could have wide-reaching implications for quantitative cancer receptor imaging using any imaging modalities, or combinations of imaging modalities, capable of concurrent detection of at least two distinct imaging agents (e.g., SPECT, optical, and PET/MR). [DOI: 10.1117/1.JBO.23.6.066004]

Keywords: paired-agent imaging; kinetic modeling; optical tissue properties.

Paper 180056R received Jan. 25, 2018; accepted for publication May 31, 2018; published online Jun. 21, 2018.

1 Introduction

The development of more quantitative methods to noninvasively measure drug-targetable biomolecules in cancerous tissues could significantly assist the advancement of precision medicine.[1] Overexpressed cancer cell surface receptors serve as strong prognostic biomarkers in a spectrum of solid tumors. Accordingly, targeting cell surface receptors has become a major focus for molecular imaging and therapy.[2] Targeted imaging agents can detect the overexpressed receptors on the surface of cancer cells dynamically through noninvasive imaging techniques at least qualitatively.[3] Applying quantitative analyses to the qualitative imaging data would potentially establish a standard identification tool to select the targeted drug for individual patients. For example, epidermal growth factor receptor (EGFR), a receptor that is overexpressed on the surface of many cancerous cell types, controls cellular proliferation by its tyrosine kinase signalling pathways.[4] As a result, quantifying the concentration of available EGFR receptors could assist in guiding the use of therapies capable of targeting these pathways.[5] Recently, paired-agent imaging techniques have been demonstrated to be able to quantify cancer cell surface receptors *in vivo*.[6,7] In these methods, an untargeted "control" imaging agent with chemical characteristics similar to the targeted agent is coadministered with the targeted imaging agent. The signal of the control agent can then be used to account for the effects of hemodynamics and nonspecific uptake and retention on the targeted imaging agent signal, allowing the binding kinetics to be isolated.[8] To image both the targeted and control agent signals concurrently in optical imaging applications, the two agents are typically labeled with different fluorophores that have distinguishable excitation and emission peak wavelengths, allowing for signal discrimination based on relatively straightforward filtering. Therefore, to convert the fluorescence signal intensities to their respective imaging agent concentrations in tissue, different correction factors (represented as η_T and η_C for the targeted and control imaging agents, respectively) must be considered for each imaging agent.

The correction factor differences are affected by a number of parameters: including the power of the light source at the respective excitation wavelengths, the sensitivity of the detector(s) at the respective emission wavelengths, the quantum efficiencies of the respective fluorophores used, and the differences in tissue optical properties at the respective excitation/emission wavelengths. Although light source, detection efficiency, and quantum efficiency effects can be accounted for by imaging a calibration standard/solution of known fluorophore concentrations with the system employed, accounting for optical property effects is more complicated. Tissue optical properties in the near-infrared are dominated by blood volume and oxygenation, and photon scatter, factors that can be spatially heterogeneous, particularly in cancerous tissues or around cancer margins, owing to the abnormal effects cancers have on angiogenesis and vasculogenesis.[9] In previous work, a pixel-by-pixel normalization was developed to account for differences in the

*Address all correspondence to: Kenneth M. Tichauer, E-mail: tichauer@iit.edu

1083-3668/2018/$25.00 © 2018 SPIE

correction factors.[10] This method assumed that the control and the targeted signals should be equal to each other in all locations at a very early time point after injection (<2 min), as preferential retention of the targeted agent in regions overexpressing the targeted biomolecule would not be evident until the washout phase. One of the problems with pixel-by-pixel normalization is that it is highly dependent on the time of normalization after administration of the imaging agents, as demonstrated in this work, and it also assumes that the more dynamic first pass kinetics of the targeted and control agents are equivalent.

In this study, we present a kinetic model we have named the "linearized scaling factor simplified paired-agent model" ($SPAM_{SF}$) in reference to its similarity to the simplified reference tissue model, SRTM,[11] and specifically the linearized version of the model,[12] widely used in positron emission tomography (PET) studies. One key difference of all paired-agent applications is the replacements of the reference tissue input with the colocalized reference (control) imaging agent signal input. This is typically employed predominantly for cancer imaging owing to the difficulty in selecting suitable reference tissues for cancer.[13] Existing paired-agent kinetic modeling methods based on SRTM require the targeted and control imaging agent signals as a function of time to estimate three parameters: R_1, the ratio of extravasation rate constants for the targeted and control agents ($K_{1,T}/K_{1,C}$); $k_{2,T}$, the tissue-to-blood efflux rate constant of the targeted agent; and BP, the "nondisplaceable" binding potential, a parameter that is proportional to the product of the targeted imaging agent affinity and the concentration of the targeted biomolecule.[14] However, in $SPAM_{SF}$, it is assumed that $R_1 = 1$, and instead the ratio of $\alpha = \eta_T/\eta_C$ is incorporated as a fitting parameter. Computer simulations and mouse models of human cancer were employed to establish the validity of BP estimation with $SPAM_{SF}$, and its precision and accuracy were compared with linearized SRTM directly applied to paired-agent data (SPAM) and the pixel-by-pixel normalization SPAM method ($SPAM_{PN}$).

Here, we present a pure blind identification method termed the "multiple reference tissue method" (MRTM). As in other approaches, the MRTM utilizes two or more reference tissues to estimate the AIF, but in this case assumes only that the AIFs in the reference tissues have the same shape, with a possible difference in bolus arrival time. Importantly, the MRTM is a mathematical framework equipped with efficient algorithms that can be applied to any kinetic model, including nonlinear models, and to any CE imaging modality. The constructed AIF is smooth and has high temporal resolution. Because there is no limitation on the kinetic models that can be utilized, the tumors themselves can be used as a source of reference tissues. In fact, the inherent heterogeneity of tumors can be exploited by utilizing individual subregions with different properties as "reference tissues." This ability avoids the necessity of including multiple normal reference tissues in the FOV.

2 Theory

Paired-agent kinetic modeling is designed to estimate binding potential (BP)—a parameter directly proportional to the targeted receptor concentration—in molecular imaging studies, and in particular, cancer molecular imaging studies.[7] To accurately extract quantitative parameters, the dynamic behavior of a targeted and control imaging agent pair can be represented by a system of equations, assuming "trace" concentrations of the targeted imaging agent and instantaneous spatial mixing of imaging agent concentrations in each "compartment" as defined by the model in Fig. 1[15]

$$\frac{dC_{f,T}(t)}{dt} = K_{1,T}C_{p,T}(t) - (k_{2,T} + k_{3,T})C_{f,T}(t) + k_{4,T}C_{b,T}(t), \tag{1}$$

$$\frac{dC_{b,T}(t)}{dt} = k_{3,T}C_{f,T}(t) - k_{4,T}C_{b,T}(t), \tag{2}$$

$$\frac{dC_{f,C}(t)}{dt} = K_{1,C}C_{p,C}(t) - k_{2,C}C_{f,C}(t), \tag{3}$$

$$\mathrm{ROI}_T(t) = \eta_T[v_p C_{p,T}(t) + C_{f,T}(t) + C_{b,T}(t)], \tag{4}$$

$$\mathrm{ROI}_C(t) = \eta_C[v_p C_{p,C}(t) + C_{f,C}(t)], \tag{5}$$

where $C_{p,T}(t)$ and $C_{p,C}(t)$ represent the blood plasma concentrations of the targeted and control imaging agents as a function of time, t; $C_{f,T}(t)$ and $C_{b,T}(t)$ represent the concentrations of

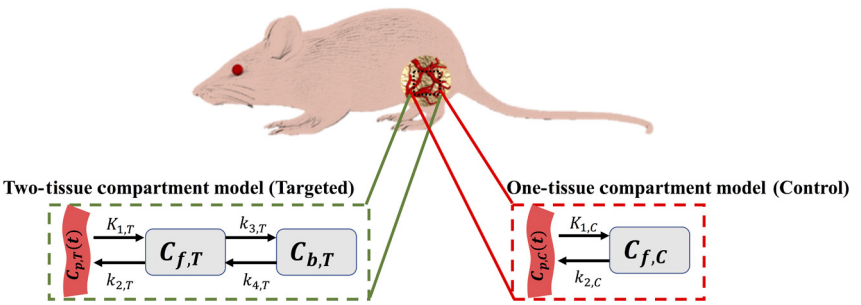

Fig. 1 A schematic of subcutaneous mouse tumor model is shown. The targeted and control imaging agent compartmental models are shown on the left and right, respectively. $C_{p,T}(t)$ and $C_{p,C}(t)$ represent the blood plasma concentrations of targeted and control imaging agents, respectively, as a function of time, t; $C_{f,T}$ and $C_{f,C}$ represent the free (unbound) concentrations of the two imaging agents, $C_{b,T}$ represents the bound concentration of the targeted agent; $K_{1,T}$ and $K_{1,C}$ represent rate constants governing targeted and control imaging agent extravasation (transport from blood to extravascular extracellular space); $k_{2,T}$ and $k_{2,C}$ represent rate constants governing targeted and control agent tissue efflux (transport from extravascular extracellular space to blood); and $k_{3,T}$ and $k_{4,T}$ represent rate constants governing targeted agent binding and dissociation from the targeted biomolecule.

the targeted agent in free and bound spaces/compartments, respectively; $C_{f,C}(t)$ represents the concentration of the control imaging agent in the free space; $K_{1,T}$ and $K_{1,C}$ are the rate constants governing extravasation of targeted and control imaging agents, respectively, from blood plasma to the free space; $k_{2,T}$ and $k_{2,C}$ are the rate constants governing efflux of the targeted and control imaging agents, respectively, from free space to the plasma; $k_{3,T}$ and $k_{4,T}$ are the rate constants governing targeted imaging agent binding and dissociation from targeted receptors/biomolecules; $\mathrm{ROI}_T(t)$ and $\mathrm{ROI}_U(t)$ represent the measured signals from the targeted and control agents, respectively, in a region-of-interest; η_T and η_C represent the correction factors relating tissue concentration to detected signal for the targeted and control agents, respectively; and v_p is the blood plasma volume fraction in the region-of-interest (volume of blood plasma/volume of region-of-interest).

Three main assumptions are typically made to solve the system of differential equations in Eqs. (1)–(3), which are nearly identical to those employed in widely used reference tissue modeling:[14] (1) the free and bound concentrations of the targeted imaging agent are in rapid equilibrium (known as the adiabatic approximation), such that Eqs. (1) and (2) can be combined into a single compartment equation;[11] (2) the magnitude of any imaging agent signal arising from the plasma compartment is negligible compared with the signal arising from the tissue compartments;[11] and (3) the ratios of the rate constants of extravasation and tissue efflux are the same between targeted and control imaging agent models (i.e., $K_{1,T}/k_{2,T} = K_{1,C}/k_{2,C}$). Such assumptions have led to the derivation of the linearized simplified reference tissue model (commonly referred to as SRTM) that is employed primarily in brain PET studies[12] but that has also been evaluated for paired-agent imaging,[16] which is referred to as the simplified paired-agent model (SPAM) in this work and is expressed as

$$\mathrm{ROI}_T(t) = R_1\mathrm{ROI}_C(t) + k_{2,T}\int_0^t \mathrm{ROI}_C(u)\mathrm{d}u - \left(\frac{k_{2,T}}{1+\mathrm{BP}}\right)\int_0^t \mathrm{ROI}_T(u)\mathrm{d}u, \tag{6}$$

where u is a dummy variable of t, $R_1 = K_{1,T}/K_{1,C}$ and $\mathrm{BP} = k_{3,T}/k_{4,T}$ is the nondisplaceable "binding potential" that is directly proportional to the targeted biomolecule,[14] and is therefore the key parameter of interest in this type of modeling. If ROI_T and ROI_C are known/measured, R_1, $k_{2,T}$, and BP can all be estimated explicitly through least squares regression of Eq. (6).

Paired-agent imaging requires that two additional assumptions be accurate for SRTM to be adopted for BP estimation: (1) that the plasma input functions of the targeted and control agents be similar (i.e., $C_{p,T} = C_{p,C}$)—however, methods for correction if this equivalence is not true have been developed[17]—and (2) that the correction factors relating tissue concentration to detected signal for both the targeted (η_T) and control (η_C) imaging agents be known/calculated, or at least that the ratio of the two correction factors (η_T/η_C) be known. One method of estimating the ratio of the correction factors is by assuming that the concentrations of the targeted and control imaging agents are equivalent at a very early time point, t_e, typically within 2 min of imaging agent injection.[10] Under this assumption, any differences in measured targeted and control agent signal at t_e can be attributed to differences in the correction factors, η_T and η_C, which can be affected by local optical properties, such that η_T/η_C can be represented by $\mathrm{ROI}_T(t_e)/\mathrm{ROI}_C(t_e)$. One advantage of this method is that it can be applied on a pixel-by-pixel (or region-by-region) basis such that spatial heterogeneity in optical properties (and their effects on the correction factors) can be accounted for. This pixel-normalization method can be expressed in terms of the SPAM as $\mathrm{SPAM}_{\mathrm{PN}}$

$$\mathrm{ROI}_T(t) = \frac{\mathrm{ROI}_T(t_e)}{\mathrm{ROI}_C(t_e)}\left[R_1\mathrm{ROI}_C(t) + k_{2,T}\int_0^t \mathrm{ROI}_C(u)\mathrm{d}u\right] - \left(\frac{k_{2,T}}{1+\mathrm{BP}}\right)\int_0^t \mathrm{ROI}_T(u)\mathrm{d}u. \tag{7}$$

However, $\mathrm{SPAM}_{\mathrm{PN}}$ has a few limitations. As $\mathrm{ROI}_T(t_e)$ and $\mathrm{ROI}_C(t_e)$ are collected at a single imaging time point, the variance in the ratio estimate is more sensitive to experimental noise and errors in motion correction than a multitime point normalization would be. Furthermore, binding characteristic differences between the targeted and control agents could lead to differences in tissue concentrations even at very early time points depending on the imaging agents used. As such, this work presents a scaling factor SPAM ($\mathrm{SPAM}_{\mathrm{SF}}$) that provides a more robust correction for optical property-based effects on the correction factors η_T and η_C.

2.1 *Linearized Scaling Factor Simplified Paired Agent Model*

Here, a derivation of the $\mathrm{SPAM}_{\mathrm{SF}}$ model is presented directly from Eqs. (1)–(5). First, assuming $C_{p,T}$ and $C_{p,C}$ are different, they can be related generally as

$$C_{p,T}(t) = C_{p,C}(t) * g(t), \tag{8}$$

where $g(t)$ is any function that can be convolved with $C_{p,C}$ that will match its shape to $C_{p,T}$, and * represents the convolution operator. Equation (3) can be rearranged to achieve

$$C_{p,C}(t) = \frac{1}{K_{1,C}}\frac{dC_{f,C}(t)}{dt} + \frac{k_{2,C}}{K_{1,C}}C_{f,C}(t). \tag{9}$$

Then, $C_{p,T}(t)$ can be approximated as a function of $\mathrm{ROI}_C(t)$ by combining Eqs. (8) and (9) and assuming $C_{f,C} \gg v_p C_{p,C}$ from Eq. (5) (the later assumption is often assumed for fast clearing imaging agents[11])

$$C_{p,T}(t) = \left[\frac{1}{\eta_C K_{1,C}}\frac{d\mathrm{ROI}_C(t)}{dt} + \frac{k_{2,C}}{\eta_C K_{1,C}}\mathrm{ROI}_C(t)\right] * g(t). \tag{10}$$

Concurrently, assuming the adiabatic approximation [i.e., $C_{b,T}(t)/C_{f,T}(t) = \text{constant}$], and $C_{f,T} \gg v_p C_{p,T}$ from Eq. (4), Eqs. (1) and (2) can be combined to form

$$\frac{d\mathrm{ROI}_T(t)}{dt} = \eta_T K_{1,T} C_{p,T}(t) - \frac{k_{2,T}}{1+\mathrm{BP}}\mathrm{ROI}_T(t). \tag{11}$$

Combining Eqs. (10) and (11), integrating both sides, and assuming $K_{1,T}/k_{2,T} = K_{1,C}/k_{2,C}$ produces

$$\mathrm{ROI}_T(t) = \frac{\eta_T}{\eta_C}\left[R_1\mathrm{ROI}_C(t) * g(t) + k_{2,T}\int_0^t \mathrm{ROI}_C(u) * g(u)\mathrm{d}u\right] - \left(\frac{k_{2,T}}{1+\mathrm{BP}}\right)\int_0^t \mathrm{ROI}_T(u)\mathrm{d}u, \quad (12)$$

where $K_{1,T}$ and $K_{1,C}$ are the primarily influenced by the blood flow and vascular permeability of the tissue, approximated as

$$K_1 = \left(1 - e^{-\frac{PS}{F}}\right)F, \quad (13)$$

where PS is the permeability-surface area product (leakiness of the blood vessel multiplied by blood vessel surface area) and F is the blood flow.[18] Therefore, for chemically similar targeted and control imaging agents an assumption that $K_{1,T} = K_{1,C}$ and therefore $R_1 = 1$, is likely valid, yielding $\mathrm{SPAM_{SF}}$ with plasma input function correction

$$\mathrm{ROI}_T(t) = \alpha\mathrm{ROI}_C(t) * g(t) + \alpha k_{2,T}\int_0^t \mathrm{ROI}_C(u) * g(u)\mathrm{d}u - \left(\frac{k_{2,T}}{1+\mathrm{BP}}\right)\int_0^t \mathrm{ROI}_T(u)\mathrm{d}u, \quad (14)$$

where $\alpha = \eta_T/\eta_C$. Under the condition where targeted and control agents are selected such that $C_{p,T}(t) = C_{p,C}(t)$, $g(t)$ is equal to a Dirac-delta function, $\delta(t)$, and Eq. (14) simplifies to the standard $\mathrm{SPAM_{SF}}$

$$\mathrm{ROI}_T(t) = \alpha\mathrm{ROI}_C(t) + \alpha k_{2,T}\int_0^t \mathrm{ROI}_C(u)\mathrm{d}u - \left(\frac{k_{2,T}}{1+\mathrm{BP}}\right)\int_0^t \mathrm{ROI}_T(u)\mathrm{d}u, \quad (15)$$

which can be solved explicitly using least squares to estimate α, $k_{2,T}$, and BP. If $C_{p,T}(t)$ and $C_{p,C}(t)$ are not equivalent, then $g(t)$ can either be estimated by deconvolving direct measures of $C_{p,T}(t)$ and $C_{p,C}(t)$, or by deconvolving targeted and control kinetic curves taken from a "reference" region (one devoid of target biomolecule). These methods have been described in detail previously;[17] however, there is a subtle difference in this reference region correction method that requires an additional note in the case where the ratio of correction factors (η_T/η_C) is not the same in an ROI and the reference region (REF). Briefly, Eq. (1) can be solved in the absence of binding ($k_{3,T} = 0$) for the reference region, REF_T

$$\mathrm{REF}_T(t) = \eta_{T,\mathrm{REF}}K_{1,T,\mathrm{REF}}C_{p,T} * e^{-k_{2,T,\mathrm{REF}}t}, \quad (16)$$

where $\eta_{T,\mathrm{REF}}$ represents the targeted concentration-to-signal correction factor for the reference region specifically. Similarly, Eq. (2) can be solved for the reference region

$$\mathrm{REF}_C(t) = \eta_{C,\mathrm{REF}}K_{1,C,\mathrm{REF}}C_{p,C} * e^{-k_{2,C,\mathrm{REF}}t}, \quad (17)$$

If the K_1s and k_2s again are considered equivalent in the reference region, it can be shown that the deconvolution of REF_T and REF_C will yield

$$g_{\mathrm{REF}}(t) = \alpha_{\mathrm{REF}}g(t), \quad (18)$$

where $\alpha_{\mathrm{REF}} = \eta_{T,\mathrm{REF}}/\eta_{C,\mathrm{REF}}$. Therefore, Eq. (14) must be amended slightly to

$$\mathrm{ROI}_T(t) = \frac{\alpha}{\alpha_{\mathrm{REF}}}\mathrm{ROI}_C(t) * g_{\mathrm{REF}}(t) + \frac{\alpha}{\alpha_{\mathrm{REF}}}k_{2,T}\int_0^t \mathrm{ROI}_C(u) * g_{\mathrm{REF}}(u)\mathrm{d}u - \left(\frac{k_{2,T}}{1+\mathrm{BP}}\right)\int_0^t \mathrm{ROI}_T(u)\mathrm{d}u. \quad (19)$$

3 Methods

3.1 *Simulation Study*

To compare the scaling factor model, $\mathrm{SPAM_{SF}}$, with two established models, SPAM and $\mathrm{SPAM_{PN}}$, targeted and control imaging agent kinetic data were generated from an analytical solution to the compartmental model system of differential equations presented in Eqs. (1)–(3), based on parameter estimates described below and experimentally derived plasma input functions of epidermal growth factor (EGF) labeled with IRDye 800CW (LI-COR Biosciences, Lincoln, Nebraska).[19] Resulting curves were interpolated to 60-min time windows at 1-min time intervals and scaled such that the highest concentration curve in all simulated curves would be representative of 50% of signal saturation on a 16-bit detector. Assuming noise in light detection is dominated by shot-noise, Poisson noise was then added to all curves using the Matlab built-in function, poissrnd() (Mathworks, Natick, Massachusetts). "Typical" targeted and control kinetic curves were approximated by setting $K_{1,T}$ and $K_{1,C}$ to 0.13 min^{-1}, and $k_{2,T}$ and $k_{2,C}$ values to 0.08 min^{-1}, which were in the range of what was measured previously for IRDye 800CW-EGF;[13] and $k_{3,T}$ and $k_{4,T}$ values were set to 0.2 and 0.1 min^{-1} in the tumor, based on direct measures of EGF binding to its receptor, EGFR.[20,21] To evaluate the effects of differences in the concentration-to-signal correction factors, η_T and η_C, on the fitting models (SPAM, $\mathrm{SPAM_{PN}}$, and $\mathrm{SPAM_{SF}}$), α was varied over a range of 0.1 to 10 while holding all other parameters constant. For optical imaging applications, α depends on the fractional differences between the optical properties of the tissue (absorption and scattering) experienced by the light emitted from the targeted and control imaging agent, as long as all other differences in channel sensitivity are accounted for. It can vary significantly from location to location with magnitudes that will depend on a number of factors that are difficult to approximate. In a previous study mouse human xenograft study, the measured range of α was 1.5 to 2.7 for paired agents at wavelengths with very similar tissue optical properties.[10] The range was expanded here for generalization to a greater array of conditions. In addition, separate simulations were carried out holding $\alpha = 1$ and varying BP, k_2 and R_1 from 0.5 to 5.5, 0.03 to 0.1 min^{-1}, and 0.5 to 1.5, respectively. These ranges were selected from previous studies of BP measurement in a wide range of EGFR overexpressing tumor lines[6] and from tumor imaging with various sized imaging agents, measuring variability in K_1 and k_2.[22] Under all conditions, 1000 noise realizations were repeated to evaluate BP estimation accuracy and precision using the different fitting models.

To understand the effect of errors in the assumption that $R_1 = 1$ on the BP estimation of SPAM, $\mathrm{SPAM_{SF}}$, and $\mathrm{SPAM_{PN}}$, the simulations were altered for R_1 not equal to 1. As $R_1 = K_{1,T}/K_{1,C}$, so it can be manipulated by either changing $K_{1,T}$ or $K_{1,C}$ (or a combination of both). All methods were explored, yet results were only displayed for changing $K_{1,T}$ while keeping $K_{1,C}$ constant as all methods led to similar results.

3.2 *Animal Experimental Protocol*

Animal studies were performed in accordance with a protocol approved by the institutional animal care and user committee at Illinois Institute of Technology. The performance of $SPAM_{SF}$ was also investigated in a set of *in vivo* human glioma (U251) xenograft mouse model studies using two different imaging systems and two different sets of paired imaging agents to evaluate EGFR receptor status (via BP estimation). In the first group, five 6-week-old severe combined immunodeficient (SCID) male mice (Charles River, Wilmington, Massachusetts) were implanted with 10^6 U251 human glioblastoma cells (ATCC, Manassas, Virginia) subcutaneously on the left flank. Tumors were allowed to grow until they reached 5 mm in diameter. The mice were then anesthetized with an i.p. injection of ketamine-xylazine (100 mg/kg:10 mg/kg) and the skin surrounding the tumors was removed, prior to taping the mice down onto a glass slide and placement into a fluorescent imaging system (Odyssey®, LI-COR Biosciences). One nanomole of each IRDye 800CW-EGF and hydrolyzed IRDye 700DX (reacted with water at room temperature for 3 h) were injected i.v. into a tail vein and fluorescence images from 700 to 740 nm (with 685 nm excitation) and from 800 to 840 nm (with 785 nm excitation) were collected every 2 to 5 min for 60 min. In a separate study, five 6-week-old athymic nude male mice (ENVIGO, Indianapolis, Indiana) were similarly implanted with U251 tumor cells. When the tumors reached a diameter of 5 mm, the mice were anesthetized with 3% isoflurane and maintained with 1% to 3% isoflurane inhalation in 100% O_2. Tissue surrounding the tumors was then removed and the area was flushed with PBS and capped with clear plastic wrap to prevent the tissue from drying during imaging. Other areas of the mice were covered with nonfluorescent black felt to minimize sources of signal outside the tissues of interest. The mice were then fixed to the 37°C heated bed of a Pearl® Imaging System (LI-COR Bioscience), and 0.2 nanomoles each of IRDye 800CW-labeled anti EGFR Affibody (Affibody AB, Solna, Sweden) and IRDye 700DX-labeled negative-control-Affibody (Affibody AB) were injected i.v. via a tail vein. The targeted Affibody agent is a good-manufacturing-procedures (GMP) produced agent that is a product of a clinical trial at Dartmouth College,[23–27] and is referred to as ABY-029. Fluorescent images at the same wavelength ranges as defined for the Odyssey were then collected for 1 h at two-min intervals. In all experiments, a section of leg muscle in the opposing leg to the location of the tumor was exposed to act as a reference region. To further test the model on an orthotopic study, previously published fluorescence tomographic data of U251 cells implanted in mice brain was used.[28] Briefly, once brain tumors were visible through gadolinium-enhanced magnetic resonance imaging (Gd-MRI), athymic nude mice ($n = 5$) were injected via a tail vein with a cocktail of 0.2 nmol each of IRDye 800CW-anti-EGFR Affibody (targeted) and Alexa Fluor 750 labeled negative control Affibody (control) imaging agents. The mice were then imaged on an MRI-coupled fluorescence molecular tomography (MRI-FMT) system.[29] The dynamic uptake of the targeted and control imaging agent kinetics was imaged in the tumor using hard-prior reconstruction for 1 h at two-min intervals. In the Odyssey and Pearl studies, kinetic curves were extracted pixel by pixel and for whole tumor regions-of-interest using lab software created in MATLAB. $SPAM_{PN}$ and $SPAM_{SF}$ were fitted directly to targeted and control imaging agent kinetic curve pairs after correcting for potential differences in plasma input function kinetics by deconvolution of the reference region kinetic curves (see Sec. 2). No plasma input correction was carried out for tomography study as the two agents were shown to have very similar plasma curves.[28]

3.3 *Statistics*

Statistical analyses were carried out using the statistical package, SPSS (IBM®, Armonk, New York). Linear regression was employed to evaluate the strength of the correlation between the $SPAM_{SF}$ and $SPAM_{PN}$ estimates of BP in the case of no scaling factor. Statistical significance was based on $p < 0.05$. All data are presented as mean $\pm$ sd. The goodness of real data and model fits were evaluated by standard χ^2 value analyses.

4 Results

4.1 *Simulation Results*

Examples of simulated, noise-added targeted, and control imaging agent kinetics from Eqs. (1)–(3) and corresponding fits of the data using SPAM, $SPAM_{PN}$, and $SPAM_{SF}$ models to the data are presented in Fig. 2. The average of χ^2 values for all

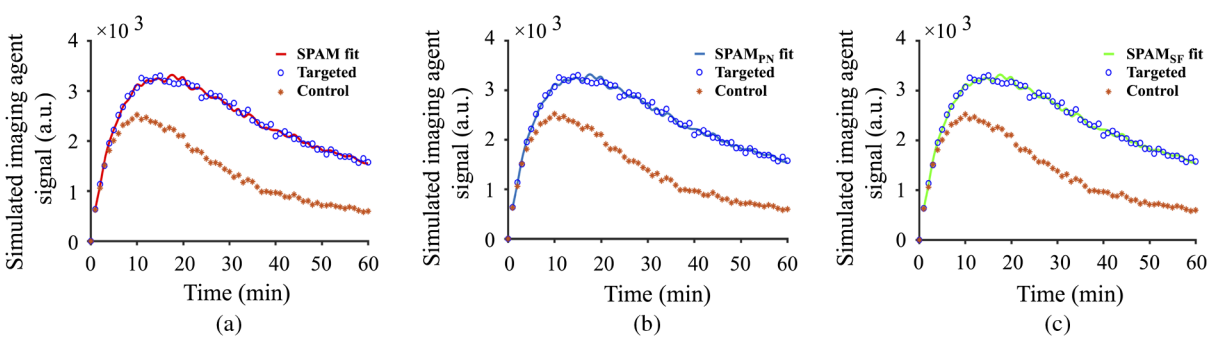

Fig. 2 Simulation results. Generated noisy targeted and control agent curves and model fits for (a) the linearized SPAM (b) the pixel-normalization SPAM ($SPAM_{PN}$), and (c) the scaling factor SPAM ($SPAM_{SF}$). The blue dots represent the targeted imaging agent signal intensity, $ROI_T(t)$. The orange dots represent the control imaging agent signal intensity, $ROI_C(t)$. Poisson noise was added to the data. The solid red, blue, and green lines represent SPAM, $SPAM_{PN}$, and $SPAM_{SF}$ fit results, respectively. The simulated values of kinetic parameters to create these simulated curves were: $K_1 = 0.013\ min^{-1}$, $k_2 = 0.08\ min^{-1}$, $k_3 = 0.2\ min^{-1}$, $k_4 = 0.1\ min^{-1}$, and $\alpha = 1$, and simulated time was 60 min.

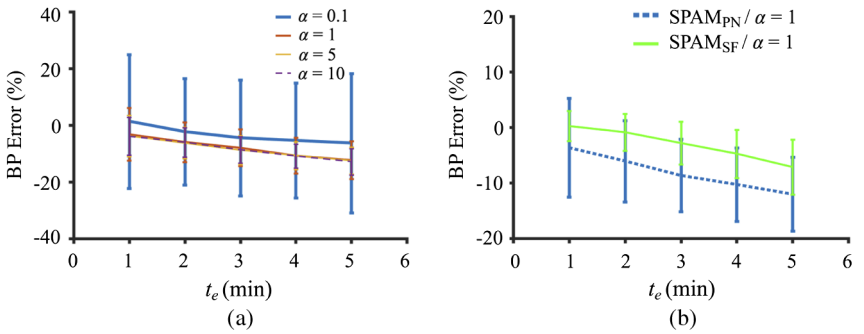

Fig. 3 Simulation results: BP estimation errors are presented for all three kinetic models tested in this study as a function of the ratios of correction factors, α (a), BP (b), the tissue-to-blood efflux rate constant, k_2 (c), and ratio of the targeted and control imaging agent blood-to-tissue extravasation rate constants, R_1 (d). The linearized SPAM results are presented in red, the pixel normalization SPAM ($SPAM_{PN}$) results are presented in blue, and the scaling factor SPAM ($SPAM_{SF}$) results are presented in green.

three model fits over a range of α from 0.1 to 10 was from 0.06 to 0.33 with all fits looking similar in quality to those displayed in Fig. 2.

Figure 3 shows a comparison of the accuracy of all three fitting models over a range of simulated parameters—specifically, α, BP, k_2, and R_1—as defined by errors in estimations of simulated BP values. In these experiments, the time point for approximating α with $SPAM_{PN}$ [t_e from Eq. (7)] was set to 1 min postimaging agent administration [Fig. 4(a) presents the effect of this selection]. While setting $R_1 = 1$, $k_2 = 0.08$ min^{-1}, and BP = 2, average errors in BP estimation for both $SPAM_{PN}$ and $SPAM_{SF}$ remained <10% for values of α between 0.1 and 10, whereas SPAM yielded average errors that were directly proportional to the percent difference in α from 1 [Fig. 3(a)]. For example, $\alpha = 1.1$ led to a 10% overestimation in BP using SPAM, whereas $\alpha = 0.5$ led to a 50% underestimation in BP. No statistically significant differences were observed between BP estimates using $SPAM_{PN}$ and $SPAM_{SF}$; however, a small negative bias in BP error using $SPAM_{PN}$ was observed, along with a variance that was more than four times larger than the error observed using $SPAM_{SF}$ ($SPAM_{PN}$ average BP error = $-3.25 \pm 9.85\%$; $SPAM_{SF}$ average BP error = $0.17 \pm 2.02\%$).

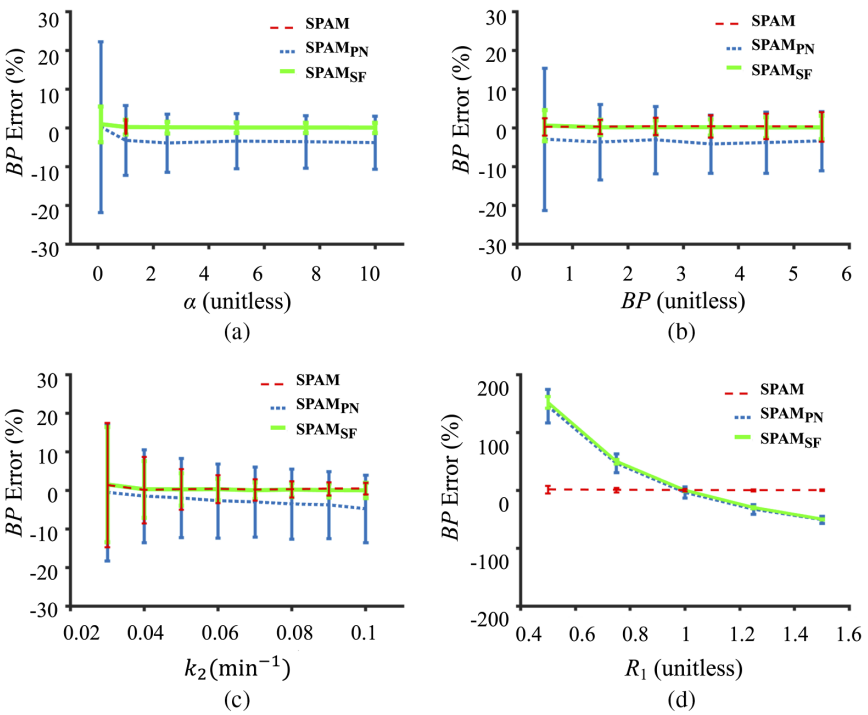

Fig. 4 Simulation results: (a) errors in BP estimation using the linearized pixel-normalization $SPAM_{PN}$ as a function of. Different colors correspond to sets of data created from different ratios of correction factors ($\alpha = \eta_T/\eta_C$). (b) Errors in BP estimation using $SPAM_{PN}$ and the SPAM scaling factor model ($SPAM_{SF}$) as a function of time-spacing of imaging data (t_e) where t_e also represents the first time point after agent administration with keeping $\alpha = 1$. $SPAM_{PN}$ and $SPAM_{SF}$ results are presented in blue and green, respectively.

At $\alpha = 1$, SPAM and $SPAM_{SF}$ were found to have equivalent performance. The magnitude of BP and k_2 had little effect on the accuracy of all three models, with $\alpha = 1$, $K_1 = 0.013$ min^{-1} [Figs. 3(b) and 3(c), respectively]. No statistically significant differences in BP estimation were observed between any of the models over a k_2 range of 0.03 to 0.1 min^{-1} and a BP range of 0.5 to 5.5. However, again there was a slight BP underestimation in $SPAM_{PN}$ that was amplified at higher k_2 values, and the variance in $SPAM_{PN}$ was more than four times that of SPAM and $SPAM_{SF}$ in all cases. Errors in the approximation that $R_1 = 1$ resulted in significant errors in both $SPAM_{PN}$ and $SPAM_{SF}$ which were inversely proportional to the scale of error in R_1 [Fig. 3(d)]. As these simulations were carried out at $\alpha = 1$, SPAM performed well for all levels of R_1 tested, with an average BP error of $0.28 \pm 3.18\%$. For testing of R_1 sensitivity, the $K_{1,T}/k_{2,T} = K_{1,C}/k_{2,C}$ equivalency was held, such that $R_1 = 1.1$ corresponded to $K_{1,T} = 1.1 * K_{1,C}$ and $k_{2,T} = 1.1 * k_{2,C}$. If only $K_{1,T}$ was changed, then $SPAM_{PN}$ and $SPAM_{SF}$ were found to be insensitive to the value of R_1, as long as $k_{2,T} = k_{2,C}$ (results not shown). However, SPAM

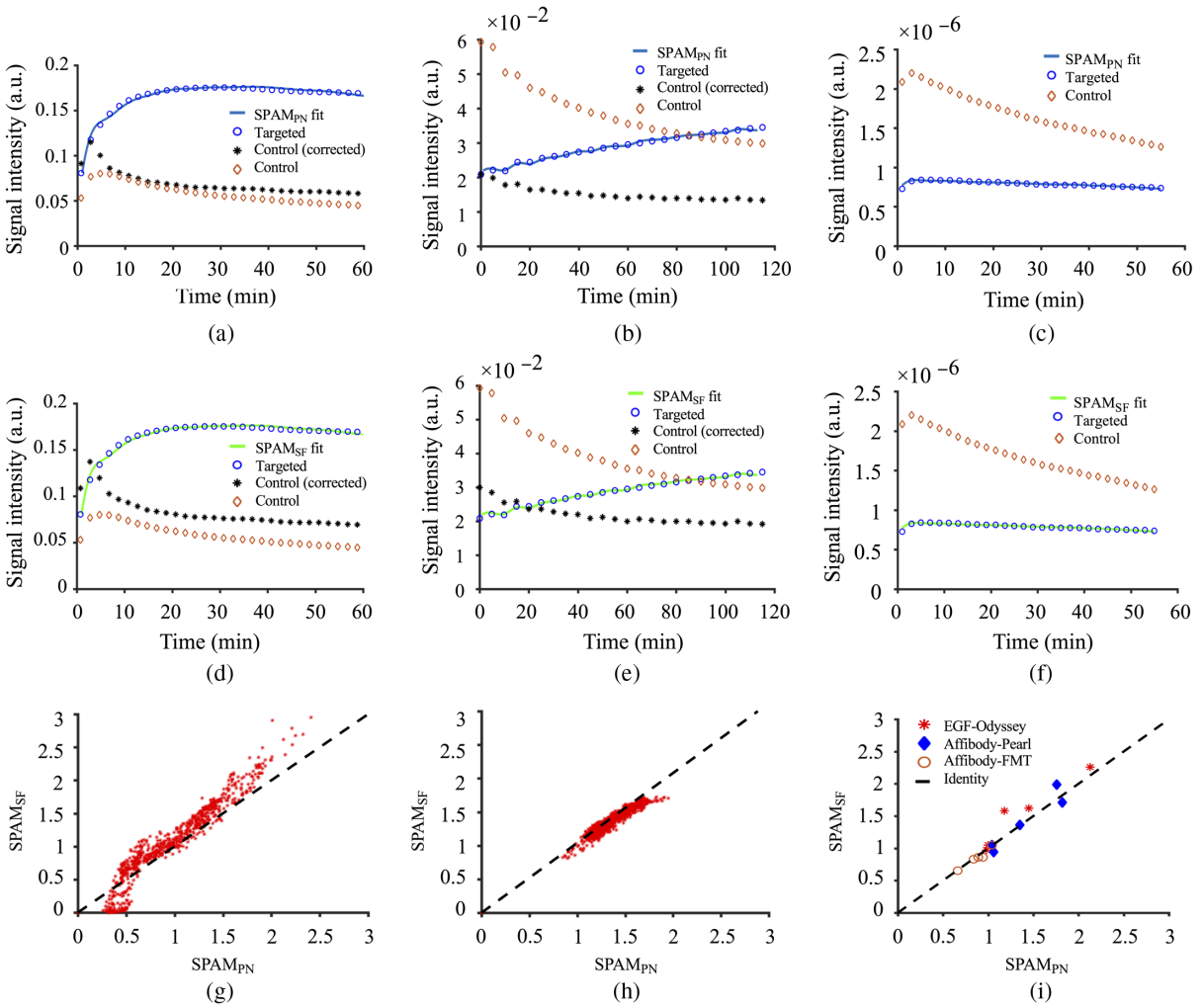

Fig. 5 *In vivo* experimental results: The linearized pixel-normalization simplified paired agent model $SPAM_{PN}$ in (a) targeted (IRDye 800CW-EGF) and control (IRDye 700DX) imaging agent signal curves measured with the Odyssey System in exposed subcutaneous human glioblastoma (U251) tumors grown in athymic mice, (b) targeted (IRDye 800CW-anti-EGFR-Affibody) and control (IRDye 700DX-negative-control-Affibody) imaging agent signal curves measured with the Pearl System in exposed subcutaneous U251 tumors and (c) targeted (IRDye 800CW-anti-EGFR-Affibody) and control (IRDye 700DX-negative-control-Affibody) imaging agent signal curves measured with an MRI–FMT system from a typical tumor region-of-interest, respectively. Corresponding model fits using the scaling factor SPAM ($SPAM_{SF}$) are presented in (d)–(f), respectively. The blue dots represent the targeted imaging agent signal intensity, the orange dots represent the control imaging agent signal intensity before correcting for plasma input function differences, the black dots represent the control imaging agent signal intensity after correcting for plasma input function differences. The solid light blue line represents the $SPAM_{PN}$ fit and the solid green line represents the $SPAM_{SF}$ fit. In (g) and (h) a pixel-by-pixel correlation of $SPAM_{SF}$ and $SPAM_{PN}$ BP estimates in all regions of an image on the same mouse data presented in (a) and (b) are presented. The dashed line is the line-of-identity. A correlation between BP values estimated by $SPAM_{SF}$ and $SPAM_{PN}$ in Odyssey, Pearl and tomography imaging studies are presented in (i) for average tumor region-of-interest fits.

exhibited errors proportional to the value of R_1 as it strictly requires that $K_{1,T}/k_{2,T} = K_{1,C}/k_{2,C}$, which is not held in this simulation (results not shown).

Irrespective of the ratio of correction factors ($\alpha = \eta_T/\eta_C$), the accuracy of $SPAM_{PN}$, defined by the error in estimation of the BP, was observed to be highly dependent on the time point after imaging agent delivery that was selected for normalization of α [Fig. 4(a)]. Specifically, the later the time point selected for normalization, the larger the underestimation in BP. Average sd in the BP estimation error at $\alpha = 0.1$ was 24.10%, and at $\alpha = 10$ was 5.13%. When normalization was carried out at 1-min post-agent-administration for $SPAM_{PN}$ at $\alpha = 1$, the average percent-error was $-3.8 \pm 6.62\%$; whereas, when carrying out the normalization at 5 min the average was $-12.67 \pm 4.72\%$. Although the $SPAM_{SF}$ requires no selected time of normalization (as the normalization is included as a fitting parameter), it was assumed that a delayed time of normalization in $SPAM_{PN}$ would only arise if data were not sampled as frequently after imaging agent administration. Therefore, the effect of data collection at a period of t_e (time of normalization for $SPAM_{PN}$) on the accuracy of $SPAM_{SF}$ was evaluated in comparison with time of normalization for $SPAM_{PN}$ [Fig. 4(b)]. For $t_e = 1$ min at $\alpha = 1$, the average percent-error of $SPAM_{SF}$ was $-0.01 \pm 1.94\%$, for $t_e = 5$ min, the average was $-7.60 \pm 3.56\%$. An increase in the error of the $SPAM_{SF}$ with data-spacing (t_e) was commensurate with the expected truncation error increase from a numerical analysis perspective. Here, SPAM was not evaluated as it resulted in identical results to $SPAM_{SF}$ since $\alpha = 1$.

Examples of targeted (IRDye 800CW-EGF) and control (IRDye 700DX) imaging agent signal curves in a typical U251 tumor are shown in Figs. 5(a) and 5(d), along with fit results using $SPAM_{PN}$ and $SPAM_{SF}$, respectively. Examples of targeted (ABY-029) and control (IRDye 700DX-negative-control-Affibody) imaging agent signal curves in a typical U251 tumor are shown in Figs. 5(b) and 5(e), along with fit results using $SPAM_{PN}$ and $SPAM_{SF}$, respectively. Examples of targeted (IRDye 800CW-anti-EGFR-Affibody) and control (IRDye 700DX-negative-control-Affibody) imaging agent signal curves in a typical orthotopic U251 tumor are shown in Figs. 5(c) and 5(f), along with fit results using $SPAM_{PN}$ and $SPAM_{SF}$, respectively. Note: SPAM fits evaluated but not displayed or discussed owing to large errors attributable to α not equal to 1 [see Fig. 3(a)]. The average goodness of the fit, quantified by χ^2, of $SPAM_{PN}$ and $SPAM_{SF}$ for all tumors were not significantly different statistically and were 0.05 ± 0.02 and 0.08 ± 0.03, respectively. The statistically significant correlation held for all individual animal datasets when BP estimation from $SPAM_{PN}$ and $SPAM_{SF}$ were compared on a pixel-by-pixel level (average $r = 0.95 \pm 0.06$, $p < 0.001$ for all cases). Examples of correlations from a single animal from the EGF-Odyssey and Affibody-Pearl groups are shown in Figs. 5(g) and 5(h), respectively. The mean $\pm$ sd of BP for $SPAM_{PN}$ and $SPAM_{SF}$ were 1.34 ± 0.47 and 1.49 ± 0.52 for the EGF-Odyssey group, respectively, 1.40 ± 0.37 and 1.41 ± 0.44 for the Affibody-Pearl group, respectively (when accounting for differences in EGF and anti-EGFR affinity), and 0.87 ± 0.14 and 0.85 ± 0.14 for the orthotopic tomography group. A statistically significant correlation was observed between BP estimates determined using $SPAM_{SF}$ and $SPAM_{PN}$ ($r = 0.98$, $p < 0.001$) when including data from all experimental groups. The correlation was not significantly different from the line-of-identity, statistically. The mean $\pm$ sd for R_1 and k_2 in all $SPAM_{PN}$ cases were 1.00 ± 0.03 and 0.07 ± 0.04 min^{-1}, respectively. The mean $\pm$ sd for α and k_2 in all $SPAM_{SF}$ cases were 0.91 ± 0.01 and 0.06 ± 0.03 min^{-1}, respectively. The BP maps from two representative mice each from the EGF-Odyssey and Affibody-Pearl groups are presented in Fig. 6.

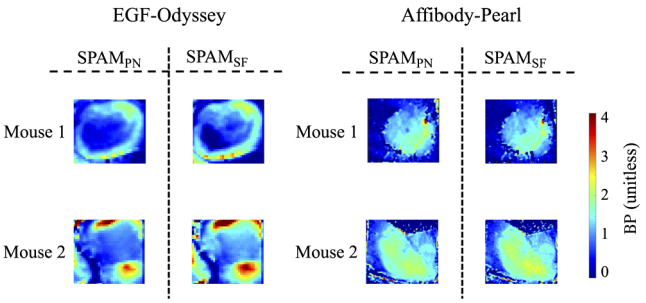

Fig. 6 *In vivo* experimental results: BP parametric maps of estimated epidermal growth factor receptor (EGFR) concentration are depicted as calculated by either the linearized pixel-normalization $SPAM_{PN}$ or the scaling factor SPAM ($SPAM_{SF}$). Here, results of four mice are displayed: two from the group imaged on the Odyssey System (targeted agent = IRDye 800CW-EGF; control = IRDye 700DX), and two from the group imaged on the Pearl System (targeted agent = ABY-029; control = IRDye 700DX-negative-control-affibody). The left two columns show the two mice imaged on the Odyssey, and the right two columns show the two mice imaged on Pearl.

5 Discussion

The development of accurate, noninvasive methods to quantify cell surface receptor concentrations in cancer molecular imaging could have far-reaching impacts on the future of precision medicine,[30] drug development,[31] and molecular guided surgery.[32] Paired-agent kinetic modeling, where the kinetics of a control (untargeted) imaging agent that is coadministered with a targeted imaging agent are used to account for nonspecific effects, has proven great promise in being capable of quantifying cancer cell surface receptor concentrations *in vivo*.[7] The paired-agent imaging kinetic models were adopted from the simplified reference tissue model (SRTM), used widely in PET studies,[14] and are referred to here as SPAM. Recently, our group derived a generalized form of SRTM and SPAM, capable of accounting for receptor saturation.[33] In this work, we present a modification to SPAM in particular, allowing the automatic correction for signal scaling differences between the detected signals of targeted and control imaging agents. This advance is particularly relevant for fluorescence imaging-based applications of SPAM, where tissue optical properties can differ heterogeneously in tissue making it difficult to accurately achieve imaging agent concentration maps of both agents.

The accuracy and precision of this scaling factor SPAM ($SPAM_{SF}$) was compared against an existing method that corrects for scaling differences between targeted and control imaging agent signals by normalizing the signals at a very early time point after agent administration[10]—assuming early signal is dominated by delivery, rather than binding, such that early targeted and control agent signals should be measured to be the same. This method is referred to here as $SPAM_{PN}$. The $SPAM_{SF}$ and $SPAM_{PN}$ models were compared both in physiologically informed, noise-added numerical simulations of targeted and control agent uptake in tumors, as well as in three different animal study groups. In each study, EGFR was targeted

by either fluorescently labeled native ligand to EGFR, EGF, or with an anti-EGFR Affibody. The results demonstrated both improved accuracy and precision of BP estimation using $SPAM_{SF}$ compared with $SPAM_{PN}$ in the simulation studies, and a strong correlation between $SPAM_{SF}$ and $SPAM_{PN}$ in the animal studies.

With respect to the simulation results, $SPAM_{PN}$ exhibited a slight underestimation in BP under all conditions tested, owing to errors in the assumption that there is no preferential retention of the targeted agent over the control agent by 1-min postinjection. In the simulation studies at least, there is some divergence of the targeted and control curves at this time, which amplified over time (Fig. 4). Furthermore, the standard deviation in the BP estimates using $SPAM_{PN}$ was found to be ~3 times larger than those found for $SPAM_{SF}$. This improvement in precision of $SPAM_{SF}$ over $SPAM_{PN}$ is attributable to the fact that $SPAM_{SF}$ essentially "fits" for the scaling factor, α, over as many time points as are in the dataset, whereas $SPAM_{PN}$ directly estimates α by normalizing targeted and control agent signals at a single time point. Therefore, it is expected that $SPAM_{PN}$ is considerably more sensitive to noise.

An additional finding from the simulation study was that errors in the assumption that $R_1 = 1$ caused significant and similar errors in the BP estimation with both $SPAM_{SF}$ and $SPAM_{PN}$: specifically, BP estimation using $SPAM_{PN}$ and $SPAM_{SF}$ was found to be inversely proportional to the scale of error in the $R_1 = 1$ assumption [Fig. 3(d)]. The sensitivity of $SPAM_{SF}$ to R_1 errors was expected because the model expressly requires $R_1 = 1$. The sensitivity of $SPAM_{PN}$ was initially difficult to explain as it fits for R_1. However, the scaling method in $SPAM_{PN}$ was found to partially normalize out R_1, which forcing an erroneous fit of true R_1, which in turn affected the accuracy in the estimation of both $k_{2,T}$ and BP.

An important assumption in all introduced models that warrants discussion is that $K_{1,T}/k_{2,T} = K_{1,C}/k_{2,C}$. The superiority of paired-agent imaging methods to conventional reference tissue models comes back to this assumption, as in conventional reference tissue imaging, it is important that the reference tissue and the region of interest have the same partition coefficients, which can be particularly difficult in cancer imaging.[13] However, in paired-agent imaging, as long as both imaging agents experience diffusion/permeability limited delivery, the $K_{1,T}/k_{2,T} = K_{1,C}/k_{2,C}$ assumption should always be accurate as both should be equivalent to the inverse of the partition coefficient. Ensuring that similar vascular permeability be experienced by both the targeted and control agents in all environments requires the agents to have similar size, charge, and lipophilicity,[22] which is true for the agents employed in this study and is generally not difficult to achieve, though should be verified by ensuring the agents have equivalent kinetics is tissues devoid of the targeted biomolecule.[6,34]

The two obvious molecular imaging modalities capable of carrying out paired-agent imaging (for application of SPAM models)—where signal for two distinct imaging agent signals must be resolvable—include SPECT and optical imaging. Considerable effort is ongoing in dual-isotope SPECT[35] to achieve signal quantification, involving correction for signal cross-talk, and photon absorption and scattering property differences in different energy windows. In SPECT, the photon absorption and scattering tissue property differences can be subtle, but they are considerably more complex in fluorescence imaging. Even so, much work has gone into designing protocols that minimize these effects. For instance, employing excitation at wavelengths with low tissue attenuation can avoid high tissue absorption by hemoglobin,[36] and multispectral fluorescence imaging can allow multiple fluorescence agents to be imaged within similar wavelength ranges.[28] Use of surface-enhanced Raman scattering nanoparticles takes this idea to the limit as multiple "flavors" of particles can be excited with the same wavelength, and their respective, unique spectral signatures can be measured over identical spectral windows such that the optical properties of excitation and emission are nearly identical.[37] Moreover, the idea of epi-illumination surface imaging, where both source and detector are focused at the same location, could minimize absorption and scattering effects by limiting the detectable fluorescence events to those close to the surface.[38] It is also possible to mitigate optical property effects by normalizing fluorescence signals to simultaneously measured excitation light signals,[39,40] or the excitation light spectrum can be employed in more sophisticated terms to quantify the optical properties.[41]

In summary, it can be stated that if the data being collected is more likely to conform to $\alpha = 1$, but R_1 not equal to 1 ("case 1"), then SPAM (which is similar to SRTM in conventional reference tissue imaging) is the model of choice. If the data is more likely to conform to $R_1 = 1$, but α is not equal to 1 ("case 2"), then $SPAM_{SF}$ is the model of choice (outperforming $SPAM_{PN}$, which is also more accurate than SPAM for "case 2"). Examples of "case 1" include studies where imaging agent concentration can be readily quantified from images such as PET neurotransmitter receptor imaging. Examples of "case 2" include studies where a control agent signal in the region of interest is used to account for agent delivery kinetics and nonspecific retention—require simultaneous imaging of two agents such as dual-isotope single photon emission tomography (SPECT) or fluorescence optical paired-agent imaging. In both modalities, accurate concentration quantification from signal is not straightforward, such that it may not be possible to ensure that $\alpha = 1$. Yet, if the targeted and control agents are designed such that they experience the same levels of blood vessel permeability (PS), based on their size, charge, and lipophilicity,[42] then it is conceivable by Eq. (13) that the $R_1 = 1$ assumption would hold. Despite the potential for signal quantification in both SPECT and optics, all of the methods require either specialized equipment or unique expertise in data analysis. The advantage of $SPAM_{SF}$—demonstrated in this work in simulations and animal studies—is that it does not require either the targeted or control imaging agent signals to be quantified. The scaling error in quantification is instead incorporated into the fitting algorithm, which is accurate as long as $R_1 = 1$ and $K_{1,T}/k_{2,T} = K_{1,C}/k_{2,C}$: conditions that are highly likely as long as the chemical properties of the targeted and control agents are similar.

Disclosures

The authors have no relevant financial interests in this article and no potential conflicts of interest to disclose.

Acknowledgments

This work was sponsored by NIH research grant R01 CA184354, NSF CAREER 1653627, and the Nayar Prize at Illinois Institute of Technology. We would also like to acknowledge Professor Brian W. Pogue and Professor Kimberley S.

Samkoe of Dartmouth College for sharing some of the animal data and the ABY-029 imaging agent.

References

1. Y. G. Assaraf, C. P. Leamon, and J. A. Reddy, "The folate receptor as a rational therapeutic target for personalized cancer treatment," *Drug Resist. Updat.* **17**(4), 89–95 (2014).
2. K. E. Henry, G. A. Ulaner, and J. S. Lewis, "Human epidermal growth factor receptor 2-targeted PET/single-photon emission computed tomography imaging of breast cancer: noninvasive measurement of a biomarker integral to tumor treatment and prognosis," *PET Clin.* **12**(3), 269–288 (2017).
3. P. M. Clark et al., "Harnessing preclinical molecular imaging to inform advances in personalized cancer medicine," *J. Nucl. Med.* **58**(5), 689–696 (2017).
4. F. B. Furnari et al., "Heterogeneity of epidermal growth factor receptor signalling networks in glioblastoma," *Nat. Rev. Cancer* **15**(5), 302–310 (2015).
5. S. L. Gibbs-Strauss et al., "Detecting epidermal growth factor receptor tumor activity in vivo during cetuximab therapy of murine gliomas," *Acad. Radiol.* **17**(1), 7–17 (2010).
6. K. M. Tichauer et al., "In vivo quantification of tumor receptor binding potential with dual-reporter molecular imaging," *Mol. Imaging Biol.* **14**(5), 584–592 (2012).
7. K. M. Tichauer et al., "Quantitative in vivo cell-surface receptor imaging in oncology: kinetic modeling and paired-agent principles from nuclear medicine and optical imaging," *Phys. Med. Biol.* **60**(14), R239–R269 (2015).
8. R. K. Jain, "Delivery of molecular and cellular medicine to solid tumors," *Adv. Drug Deliv. Rev.* **46**(1–3), 149–168 (2001).
9. J. A. Nagy et al., "Why are tumour blood vessels abnormal and why is it important to know?" *Br. J. Cancer* **100**(6), 865–869 (2009).
10. S. C. Kanick et al., "Pixel-based absorption-correction for dual-tracer fluorescence imaging of receptor binding," *Biomed. Opt. Express* **5**(10), 3280–3291 (2014).
11. A. A. Lammertsma and S. P. Hume, "Simplified reference tissue model for PET receptor studies," *Neuroimage* **4**(3 Pt 1), 153–158 (1996).
12. M. Ichise et al., "Linearized reference tissue parametric imaging methods: application to [11C]DASB positron emission tomography studies of the serotonin transporter in human brain," *J. Cereb. Blood Flow Metab.* **23**(9), 1096–1112 (2003).
13. K. M. Tichauer et al., "Advantages of a dual-tracer model over reference tissue models for binding potential measurement in tumors," *Phys. Med. Biol.* **57**(20), 6647–6659 (2012).
14. R. B. Innis et al., "Consensus nomenclature for in vivo imaging of reversibly binding radioligands," *J. Cereb. Blood Flow Metab.* **27**(9), 1533–1539 (2007).
15. M. A. Bourdon et al., "Monoclonal antibody localization in subcutaneous and intracranial human glioma xenografts: paired-label and imaging analysis," *Anticancer Res.* **4**(3), 133–140 (1984).
16. N. Hamzei et al., "Comparison of kinetic models for dual-tracer receptor concentration imaging in tumors," *Austin J. Biomed. Eng.* **1**(1), 9 (2014).
17. K. Tichauer et al., "Accounting for pharmacokinetic differences in dual-tracer receptor density imaging," *Phys. Med. Biol.* **59**(10), 2341–2351 (2014).
18. J. A. Johnson and T. A. Wilson, "A model for capillary exchange," *Am. J. Physiol.* **210**(6), 1299–1303 (1966).
19. K. S. Samkoe et al., "High vascular delivery of EGF, but low receptor binding rate is observed in AsPC-1 tumors as compared to normal pancreas," *Mol. Imaging Biol.* **14**(4), 472–479 (2012).
20. S. Felder et al., "Kinetics of binding, endocytosis, and recycling of EGF receptor mutants," *J. Cell Biol.* **117**(1), 203–212 (1992).
21. M. Zhou et al., "Real-time measurements of kinetics of EGF binding to soluble EGF receptor monomers and dimers support the dimerization model for receptor activation," *Biochemistry* **32**(32), 8193–8198 (1993).
22. Q. G. de Lussanet et al., "Dynamic contrast-enhanced MR imaging kinetic parameters and molecular weight of dendritic contrast agents in tumor angiogenesis in mice," *Radiology* **235**(1), 65–72 (2005).
23. J. T. Elliott et al., "Microdose fluorescence imaging of ABY-029 on an operating microscope adapted by custom illumination and imaging modules," *Biomed. Opt. Express* **7**(9), 3280–3288 (2016).
24. A. L. de Souza et al., "Fluorescent affibody molecule administered in vivo at a microdose level labels EGFR expressing glioma tumor regions," *Mol. Imaging Biol.* **19**(1), 41–48 (2017).
25. J. T. Elliott et al., "Simultaneous in vivo fluorescent markers for perfusion, protoporphyrin metabolism, and EGFR expression for optically guided identification of orthotopic glioma," *Clin. Cancer Res.* **23**(9), 2203–2212 (2017).
26. K. S. Samkoe et al., "Development and evaluation of a connective tissue phantom model for subsurface visualization of cancers requiring wide local excision," *J. Biomed. Opt.* **22**(12), 1–12 (2017).
27. K. S. Samkoe et al., "Toxicity and pharmacokinetic profile for single-dose injection of ABY-029: a fluorescent Anti-EGFR synthetic affibody molecule for human use," *Mol. Imaging Biol.* **19**(4), 512–521 (2017).
28. S. C. Davis et al., "Dynamic dual-tracer MRI-guided fluorescence tomography to quantify receptor density in vivo," *Proc. Natl. Acad. Sci. U. S.A.* **110**(22), 9025–9030 (2013).
29. S. C. Davis et al., "Magnetic resonance-coupled fluorescence tomography scanner for molecular imaging of tissue," *Rev. Sci. Instrum.* **79**(6), 064302 (2008).
30. R. Weissleder and M. J. Pittet, "Imaging in the era of molecular oncology," *Nature* **452**(7187), 580–589 (2008).
31. J. K. Willmann et al., "Molecular imaging in drug development," *Nat. Rev. Drug Discov.* **7**(7), 591–607 (2008).
32. R. R. Zhang et al., "Beyond the margins: real-time detection of cancer using targeted fluorophores," *Nat. Rev. Clin. Oncol.* **14**(6), 347–364 (2017).
33. N. Sadeghipour, S. C. Davis, and K. M. Tichauer, "Generalized paired-agent kinetic model for in vivo quantification of cancer cell-surface receptors under receptor saturation conditions," *Phys. Med. Biol.* **62**(2), 394–414 (2017).
34. K. S. Samkoe et al., "Quantitative in vivo immunohistochemistry of epidermal growth factor receptor using a receptor concentration imaging approach," *Cancer Res.* **74**(24), 7465–7474 (2014).
35. G. El Fakhri et al., "Absolute activity quantitation in simultaneous 123I/99mTc brain SPECT," *J. Nucl. Med.* **42**(2), 300–308 (2001).
36. K. R. Diamond, M. S. Patterson, and T. J. Farrell, "Quantification of fluorophore concentration in tissue-simulating media by fluorescence measurements with a single optical fiber," *Appl. Opt.* **42**(13), 2436–2442 (2003).
37. Y. Wang et al., "Raman-encoded molecular imaging (REMI) with topically applied SERS nanoparticles for intraoperative guidance of lumpectomy," *Cancer Res.* **77**(16), 4506–4516 (2017).
38. S. Andersson-Engels, J. Johansson, and S. Svanberg, "Medical diagnostic system based on simultaneous multispectral fluorescence imaging," *Appl. Opt.* **33**(34), 8022–8029 (1994).
39. P. A. Valdes et al., "qF-SSOP: real-time optical property corrected fluorescence imaging," *Biomed. Opt. Express* **8**(8), 3597–3605 (2017).
40. A. Soubret, J. Ripoll, and V. Ntziachristos, "Accuracy of fluorescent tomography in the presence of heterogeneities: study of the normalized born ratio," *IEEE Trans. Med. Imaging* **24**(10), 1377–1386 (2005).
41. A. Kim et al., "Quantification of in vivo fluorescence decoupled from the effects of tissue optical properties using fiber-optic spectroscopy measurements," *J. Biomed. Opt.* **15**(6), 067006 (2010).
42. J. A. Nagy et al., "Vascular permeability, vascular hyperpermeability and angiogenesis," *Angiogenesis* **11**(2), 109–119 (2008).

Negar Sadeghipour is a PhD candidate in the Biomedical Engineering Department, Illinois Institute of Technology (IIT). She received her bachelor's degree in materials science from Sharif University in 2013. Her current work focuses on the development of mathematical models to relate molecular imaging parameters to outcome in molecular-targeted cancer therapy

Scott C. Davis is an assistant professor of engineering at Dartmouth College. He holds degrees in physics, mechanical, and biomedical engineering. His research aims to develop optical imaging strategies to diagnose tissue and guide cancer therapy. Currently, he directs two National Cancer Institute-funded research projects to develop quantitative noninvasive optical molecular imaging and fluorescence

guided surgery and has published over 60 peer-reviewed articles covering optical and multimodal imaging and spectroscopy for surgical guidance, PDT, and radiotherapy dosimetry.

Kenneth M. Tichauer is an assistant professor of biomedical engineering at the Illinois Institute of Technology. He received his BSc degree in physics from the University of British Columbia and his PhD in medical biophysics from Western University. His research applies mathematical models of imaging agent delivery and binding to molecular imaging and therapy of cancer. He has published over 50 peer-reviewed articles, and his lab is currently funded by the National Science Foundation, National Cancer Institute, and the Nayar Prize at IIT.